International Journal of Multiphase Flow 177 (2024) 104849

Contents lists available at ScienceDirect

International Journal of Multiphase Flow

journal homepage: www.elsevier.com/locate/ijmulflow

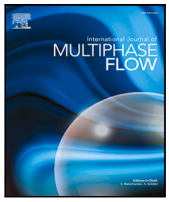

Bubble up: Tracking down the vertical velocity of oxygen bubbles in parallel plate electrolyzers using CNN

Jonas Görtz, Jakob Seiler, Andreas Jupke *

AVT.FVT - Fluid Process Engineering, RWTH Aachen University, Forckenbeckstrasse 51, 52074 Aachen, Germany

ARTICLE INFO

Keywords:
Gas-liquid flow
Particle tracking velocimetry
Convolutional neural network
Oxygen evolution reaction
Water electrolysis

ABSTRACT

Bubble-induced convection governs the flow pattern inside parallel plate electrolyzers, independent of the superficial electrolyte velocity. At the electrode surface, gas bubbles nucleate, grow and detach, increasing the gas volume fraction and accelerating the electrolyte in the proximity of the electrode. This acceleration due to buoyancy-induced bubble velocity enhances the mixing and mass transport, impacting the local concentration and, hence, the electrochemical reaction. To study the velocity and size of electrogenerated gas bubbles, we present a particle tracking velocimetry method that enables the velocity measurement directly inside the bubble curtain of a membrane-separated, parallel plate electrolyzer. By decoupling the effect of the bubble size on the bubble velocity, we study the impact of different current densities and superficial velocities of the electrolytes on the vertical bubble velocity. Our results reveal the strong dependence of the bubble velocity on the total net volume of produced gas and the thereby linked acceleration of the electrolyte near the electrode. Under no net electrolyte flow conditions, the determined vertical bubble velocities inside the bubble curtain double to triple values of single bubble experiments and predictions by commonly used drag correlations. By applying forced convection, the measured vertical velocity of equally sized bubbles decreases and shifts towards the superficial electrolyte velocity. Additionally, the horizontal bubble velocities increase at higher electrolyte velocities, indicating a broadening of the bubble curtain, as also proposed by numerical studies. The presented findings improve the understanding of gas-liquid flows in electrolyzers and, thus, the efficiency of gas-evolving parallel-plate electrolyzers.

1. Introduction

Parallel plate electrolyzers combined with gas-evolving electrodes are applied to various industrial and lab-scale electrochemical processes. Depending on the process, the electrogenerated gas bubbles are either the desired product, e.g., chlorine in chlorine-alkali, hydrogen in alkaline hydrolysis, or the by-product. Independent of the application and type of gas, the evolving gas bubbles strongly impact the process (Fuller and Harb, 2018): Bubbles attached to the electrode alter the current distribution, reducing the active surface area of the electrode (Vogt and Balzer, 2005; Eigeldinger and Vogt, 2000). Detached bubbles form a bubble curtain in proximity to the electrode, altering the electrolyte's conductivity (Mandin et al., 2008) and flow pattern due to buoyancy forces (Aldas et al., 2008). Further, due to the relative velocity between bubbles and electrolyte, pseudo-turbulence is created (Hreiz et al., 2015a), enhancing the mass transport (Janssen, 1978). Hence, the understanding of this interaction between the bubble motion and mass transport is crucial for the development and in-depth understanding of electrochemical reactors with gas-evolving reaction (Zhao et al., 2019; Sillen, 1983).

Various parameters, e.g. superficial electrolyte velocity u_{el}^{0}, bubble size d_b and gas production rate $\dot{V}_g$, affect the bubble motion inside parallel-plate electrolyzers (Boissonneau and Byrne, 2000). In general, parallel-plate electrolyzers are either operated with a forced convective flow (FCF, $u_{el}^{0} > 0\,\mathrm{mm\,s^{-1}}$) or under no net flow (NNF, $u_{el}^{0} = 0\,\mathrm{mm\,s^{-1}}$) conditions (Hreiz et al., 2015b). $\dot{V}_g$ is directly linked to the current density i by Faraday's law of electrolysis

$$\dot{V}_g = \frac{i\,A}{\rho_g\,z\,F}\,, \tag{1}$$

with the surface area of the electrode A, Faraday's constant F, the gas density ρ_g and the amount of exchanged electrons (e^-) in the reaction z. In the case of the oxygen (O_2) evolution reaction

$$2H_2O \longrightarrow O_2 + 4H^+ + 4e^-\,, \tag{2}$$

z is equal to four. The distribution of d_b varies depending on the reaction systems and operating parameters with i being the key parameter (Janssen et al., 1984; Boissonneau and Byrne, 2000; Görtz et al., 2024). and cannot be directly estimated.

* Corresponding author.
E-mail address: andreas.jupke@avt.rwth-aachen.de (A. Jupke).

https://doi.org/10.1016/j.ijmultiphaseflow.2024.104849
Received 4 January 2024; Received in revised form 21 March 2024; Accepted 29 April 2024
Available online 3 May 2024

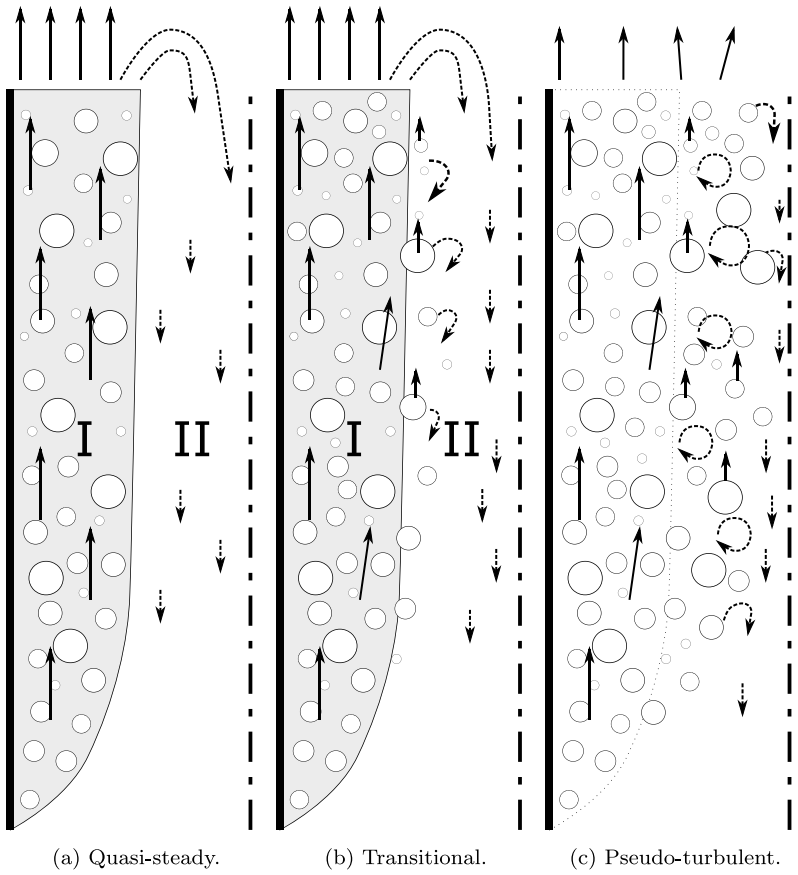

Fig. 1. Scheme of the three different electrolyte flow patterns based on i under NNF conditions. Dashed vectors indicate bubble-induced reflux or pseudo-turbulence of the electrolyte (Alexiadis et al., 2011b,a, 2012).

For different parameter sets of i, u_{el}^{0}, estimated values for d_b, and reactor geometries, analytical (Aldas et al., 2008; Rajora and Haverkort, 2022, 2023) and Computational Fluid Dynamic(CFD)-based studies (Hreiz et al., 2015b; Liu et al., 2015, 2018; Wosiak et al., 2022) investigated the effect of electrogenerated bubbles on the flow pattern inside parallel plate electrolyzers. For NNF-conditions, three alternating flow pattern are reported for different i (Alexiadis et al., 2011b,a, 2012; Rajora and Haverkort, 2023) and schematically represented in Fig. 1:

(a) At low current densities, two 'quasi-steady' regimes exist. The first regime, the bubble curtain, contains the vast majority of bubbles and exhibits larger velocities than the second regime, the bulk electrolyte. (b) The flow pattern 'transitional' present at moderate current densities predicts an oscillation of the bubble curtain. Bubbles start to detach from the electrodes and depart into the bulk electrolyte, resulting in transitory vortices. (c) By increasing the current density further, the flow pattern changes to 'pseudo-turbulent'. Due to an increase in bubble number density, average size and collision frequency, the bubble curtain widens and ultimately, vanishes. The bubble-induced, chaotic fluid motion consists of stable vortices that rotate in alternating directions. Further, Mat and Aldas (2005) and Alexiadis et al. (2011a) reported the formation of a recirculation of the electrolyte due to the liquid turnaround at the free top surface depending on the vertical bubble velocity u_b. By applying a FCF, numerical and experimental investigations by Aldas et al. (2008) show that the residence time and volume fraction of bubbles between the electrodes increases compared to NNF conditions.

The experimental evaluation of these numerical findings is challenging (Hreiz et al., 2015b): The small inter-electrode gap complicates the study of the bubble motion and the two-phase flow. Especially inside the bubble curtain and at industrial current densities ($0.1\,A\,cm^{-2}$), commonly used velocimetry methods struggle or fail to measure u_b:

(i) Particle image velocimetry (PIV) comprises of the illumination and recording of the flow twice for a small time interval and calculating the velocity of small segments of the image. Due to the overlapping bubbles on the 2D-image, Boissonneau and Byrne (2000) have failed to measure u_b. Kuroda et al. (2008) have employed a cross-correlation PIV technique developed by Cheng et al. (2005) for u_b in fields with high bubble number densities and have applied this algorithm to a small electrolytic cell. Using their algorithm, they have measured time-averaged rising velocities between 15 and $70\,mm\,s^{-1}$ for different current densities and cell widths. Similarly, Hreiz et al. (2015a) have conducted a comparable approach to study u_b in narrow vertical electrochemical electrolyzer. In order to be able to apply the PIV algorithm on taken photography, they have performed many image pre-processing steps, as well as averaging over several frames. The resulting average velocities are between 0 and $20\,mm\,s^{-1}$ and are significantly smaller than the results of Kuroda et al. (2008). Though, through time-averaging, both methods are not capable of reliably reporting the bubble velocity distribution and distinct velocity of a single bubble nor measuring the bubble size distribution. (ii) The use of laser Doppler velocimetry (LDV) is limited by the numerous side reflections introduced at high gas volume fractions (Hreiz et al., 2015a). Abdelouahed (2013) has not been able to reflect the increase in velocity alongside the height of the electrode that has been observed by manually tracking the particle. Boissonneau and Byrne (2000) have also employed a back-scatter LDV and recorded flow velocities between 4 and $120\,mm\,s^{-1}$. Nonetheless, their setup has not been able to capable of recording the velocity close to the electrode. (iii) Davis et al. (2019) have examined the rising velocity of between 15 to 20 hydrogen bubbles in a membraneless electrolyzer by using an adapted particle tracking velocimetry (PTV) algorithm. Depending on the bubble size, they report values between 10 (d_b = 50 µm) up to $130\,mm\,s^{-1}$ (d_b =

550 µm). A manual PTV method has also been utilized by Abdelouahed et al. (2014a), resulting in velocities between 5 to 30 mm s^{-1}. However, only small bubbles that escaped the bubble curtain were measured.

Besides optical approaches, other works (Pyle and Harrison, 1967; Sigrist et al., 1979, 1980; Kreysa and Kuhn, 1985) employed conductivity measurements in electrochemical reactors to estimate the u_b: By applying Bruggemanns law (Bruggeman, 1935) to the measured conductivity at different operating conditions and heights, the gas volume fraction is calculated. Subsequently, the superficial gas velocity u_g^0 can be calculated by using the cross-sectional area and $\dot{V}_g$. Finally, u_b is determined by dividing u_g^0 with the gas volume fraction (Sigrist et al., 1980). To reliable predict u_b using the gas volume fraction and vice versa, the equation

$$u_b = u_g^0 + u_{el}^0 + u_{b,sw} \tag{3}$$

based on the work of Nicklin (1962) is often employed. $u_{b,sw}$ represents the rise velocity for bubble swarms due to buoyancy forces that can be estimated by correlations, e.g., Richardson and Zaki (1954). The Nicklin equation incorporates the assumption that the present gas phase reduces the cross-area, leading to an increased liquid phase velocity. Thereby, it 'corrects' the error introduced by simply superpositioning the superficial velocities of liquid and gas phases. Using this method, Sigrist et al. (1980) experimentally determine bubble velocities between 110 and 250 mm s^{-1} at $u_{el}^0 = 21$ mm s^{-1} and report an increase of u_b with increasing u_{el}^0. While the Nicklin correlation can reflect these experimental findings, its application is limited to well-mixed systems since it holds the basic assumption of an ideally dispersed two-phase flow. However, the assumption of an ideally dispersed two-phase flow does not hold for parallel plate electrolyzers (Alexiadis et al., 2012).

In our study, we combined our previously developed (Görtz et al., 2024) partially transparent parallel plate electrolyzer setup with a high-resolution (5k), high-speed camera to study the velocity of electrogenerated oxygen gas bubbles at different heights, i and under NNF and FCF conditions. Contrarily to the above-mentioned works that focused on the small electrode gap, our setup enables the recording of the u_b directly inside the bubble curtain. The slicing of three viewing panels into the lid and electrode allows for taking 2D-images from a different angle and disentangling the bubbles in the curtain. Thus, we can overcome the previously described limitation caused by overlapping bubbles, allowing the measurement of u_b within the bubble curtain.

To determine u_b, we adopted a two-dimensional, four-frame, forward–backward PTV algorithm from Vukasinovic et al. (2004). The required positions and sizes in each frame of the electrogenerated gas bubbles are determined using our region-based convolutional neural network (R-CNN) implementation (Sibirtsev et al., 2023). This R-CNN implementation allows a robust object detection of bubbles even at high bubble number density (Poletaev et al., 2020) and shows enormous potential compared to other computer vision algorithms (Ilonen et al., 2018). Applying the combined R-CNN and PTV algorithm to the obtained images we can measure the vertical and horizontal bubble velocity and distribution for the three viewing panels at different current densities and superficial electrolyte flow velocity alongside the bubble size. The tuple of u_b and d_b enables the discussion of the effect of bubble size on the velocity distribution. Additionally, by tracking the bubbles over a series of frames, our method determines the acceleration of each bubble. Our study evaluates u_b at NNF conditions for three different current densities. Subsequently, the impact of different u_{el} on u_b is studied for three current densities.

2. Material and methods

The anode and cathode solution utilized in the experiments consists of sodium sulfate (Na_2SO_4, > 99 wt.%) sourced from Acros Organics BKBA (Geel, Belgium), succinic acid (H_2SA, > 99 wt%) and di-sodium succinic acid (Na_2SA, > 96 wt%), both from Sigma Aldrich (St. Louis, USA). The concentration of the anolyte and cathode solutions are listed in Table 1. The conductivity of the in-house produced deionized water for preparing the electrolyte solutions is measured to be smaller than 0.7 µS cm^{-1}. Vink König Deutschland GmbH (Gilching, Germany) supplied the PMMA for the lid and the flow frames. Ruthenium mixed metal-coated titanium is employed as anode material and is provided by Magneto Special Anodes B.V. (Schiedam, The Netherlands). Laser-cut Nickel 205 (99.6 wt% Nickel) is supplied by Teprosa GmbH (Magdeburg, Germany) and employed as cathode.

Table 1
Composition of anode and cathode solution for the conducted experiments.

	$c_{Na_2SO_4}$ (mol L^{-1})	c_{Na_2SA} (mol L^{-1})	c_{H_2SA} (mol L^{-1})	pH (–)
Anode	0	0.3	0	6.99
Cathode	0.5	0	0.35	2.2

2.1. Experimental setup

The experiments have been conducted in a partially transparent parallel plate electrolyzer with custom-made electrodes with three viewing panels (Görtz et al., 2024). The lid and flow frame of the anode are made of transparent 8 mm thick PMMA, allowing lighting and observation of the electrogenerated gas bubbles. The mirrored frames of the cathode are opaque to prevent cathodic-produced gas bubbles from interfering with the images. The two chambers are separated using a Nafion 117 membrane from Frontis Energy (Probstzella, Germany). Fig. 2(a) depicts the fluid flow of the electrolyte. Through the in- and outlets at the front and back of the electrolyzer, electrolytes can be pumped from the bottom to the top of the cathode and anode chamber using two MCP Standard peristaltic pumps from Cole-Parmer GmbH (Wertheim, Deutschland). Thereby, the electrolyte passes the three viewing panels, bottom, middle and top that are shown in Fig. 2(b) alongside the geometry of the custom-made electrode. The outer rim of the electrode is used to seal the chamber and does not contact the electrolyte and the active surface area of the electrode amounts to 117 cm^2.

Images are taken from the center of each viewing panel using the monochromatic high-speed camera XSream Mini 5k (5120 × 2880 pixels) from Imaging Solutions GmbH (Eningen unter Achalm, Germany). Combining the sensor with a size of 17.92 × 10.08 mm and the telecentric lens LM1119TC from Kowa Optimed Deutschland GmbH (Düsseldorf, Germany) with a demagnification of 0.7x, the pixel size results in 5 µm. Bar lights are placed at the left and right side of the transparent part of the electrolyzer as well as below and above the viewing panel at an angle of approximately 30°. By adjusting the intensity of each bar light, all edges of the bubbles can be evenly lit. To enable the vertical shift of the camera system and the bar lights, guide rails made from metal and 3D-printed polyethylene-terephthalate-glycol from Das Filament (Emskirchen, Germany) are used, respectively.

2.2. Experiments and image acquisition

At the start of each experiment, the anode and cathode chamber is flushed with new electrolyte solution from storage containers. The position of the camera and lighting system is adjusted, and the peristaltic pumps' desired volumetric flow rate and current density are set via a LabView® interface. Subsequently, images are recorded for 10 s with a frame rate of 200 s^{-1}. In preliminary studies, we found that post-processing the last 500 out of the total 2000 images is a sufficiently large subset to resemble the entire data of all images. Hence, the last 500 images are analyzed for each process condition and viewing panel.

In order to investigate the effect of different current densities and, hence, the volume of the generated oxygen on u_b in an parallel plate electrolyzer at NNF ($u_{el}^0 = 0$ mm s^{-1}) conditions, three different i of 0.01, 0.05 and 0.1 A cm^{-2} are examined. Thereafter, u_b is measured

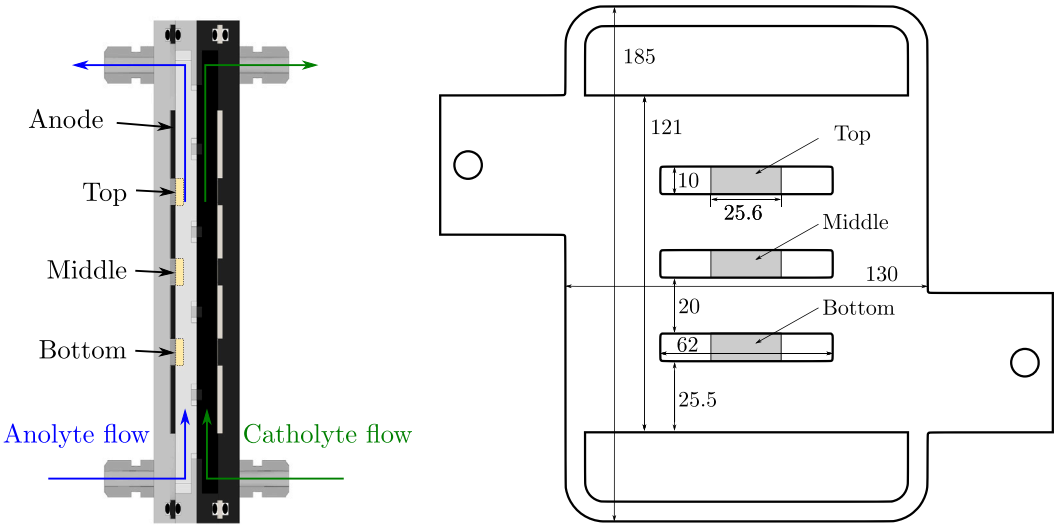

(a) Fluid flow through electrolyzer. (b) Geometry of anode.

Fig. 2. Visualization of the fluid flow through the electrolyzer and geometry of the custom-made anode. Top, middle and bottom refer to the three viewing panels. *Source:* Adapted from Görtz et al. (2024).

for the three different i with u_{el}^{0} of 10 and 20 mm s^{-1} to study the effect of convection on u_{b}. In our setup, an u_{el}^{0} of 10 and 20 mm s^{-1} is equivalent to a volumetric flow rate of 537.6 and 1075.3 ml min^{-1}. Images were acquired at the three different viewing panels for each set of experimental conditions.

2.3. PTV-algorithm

In this work, the four-frame, forward–backward PTV algorithm by Vukasinovic et al. (2004) is adapted and implemented to measure the velocity in horizontal and vertical dimensions: First, the positions and sizes of the oxygen bubbles in an image are determined using the neuronal network R-CNN. We trained the neuronal network on an image set, containing 40 pictures with on average 70 bubbles from experiments with different i and u_{el}^{0}. Here, we flipped, rotated, mirrored, and used filters on the images to prevent overfitting (Görtz et al., 2024). The algorithm determines the bounding boxes with the width x and height y for each detected bubble and calculates the bubble size as $\sqrt{xy}$. Next, bubbles that exceed an aspect ratio $x : y$ or collide with an edge of the image are discarded. For each remaining bubble, an object is created and a list of all objects is stored in a queue. This queue contains only the bubbles from the current image $n + 2$ and the last three, $n + 1$, n and n-1 images. Each time the algorithm detects gas bubbles in a new image, the entries of the last images are deleted from the queue. Subsequently, the stored data of the queue is processed using the four-frame, forward–backward PTV algorithm as illustrated in Fig. 3.For each bubble in the base image n, the algorithm searches for bubbles within a radius $r_{1,\max}$ around the center position of the bubble in the one-frame forward image $n + 1$. Additionally, the bubble sizes are compared and bubbles that exceed the maximal relative size deviation $s = d_{\mathrm{b},n+1}/d_{\mathrm{b},n}$ are filtered. For all matching pairs of bubbles, the traveled distance is calculated and the trajectory is projected into the two-frames forward $n + 2$ and one-frame backward n−1 image matches. If the position of a bubble in either the two-frames forward or one-frame backward frame matches the projected position from the previously determined trajectory with a maximal deviation of $r_{2,\max}$, the matching bubbles are stored. Again, the bubble size is checked for consistency and a lower threshold, $r_{1,\min}$, is applied to discard bubbles stuck to the PMMA. Without the minimal threshold value, stuck bubbles would be detected in each series of frames, skewing the velocity distribution. Finally, the vertical velocity and angle of descent are calculated and stored for each bubble in an object list based on the

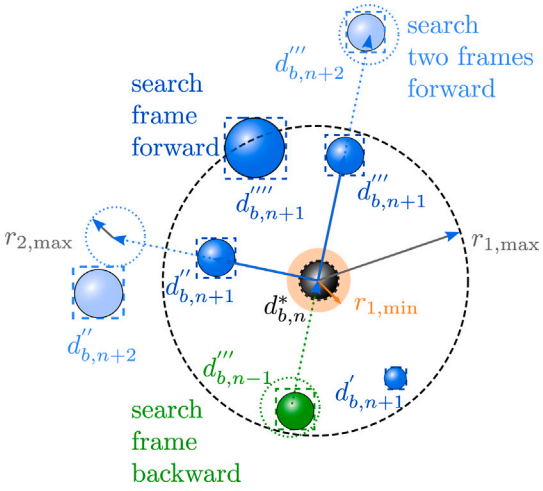

Fig. 3. PTV-algorithm and illustration adopted from Vukasinovic et al. (2004).

Table 2
Parameters for the four-frame, forward–backward PTV-algorithm.

Parameter	Value
$x : y$	$0.8 \leq x : y \leq 1.2$
s	$0.9 \leq s \leq 1.1$
$r_{1,\min}$	8 px (=8 mm s^{-1})
$r_{1,\max}$	120 px (=120 mm s^{-1})
$r_{2,\max}$	8 px (=8 mm s^{-1})

positions at the base n and one-forward $n + 1$ frame. Here, the angle α is defined as

$$\alpha = \arctan\left(\frac{u_{\mathrm{b,horizontal}}}{u_{\mathrm{b,vertical}}}\right), \tag{4}$$

where an angle of zero corresponds to a bubble moving exclusively vertically. If the velocity of a bubble is determined in successive images, it gets added to the same object, enabling the tracking of bubbles and calculation of acceleration over a series of frames. Here, the acceleration a is calculated by $a = \left(u_{b,n+1} - u_{b,n}\right)/\Delta t$. All used PTV-parameters are displayed in Table 2.

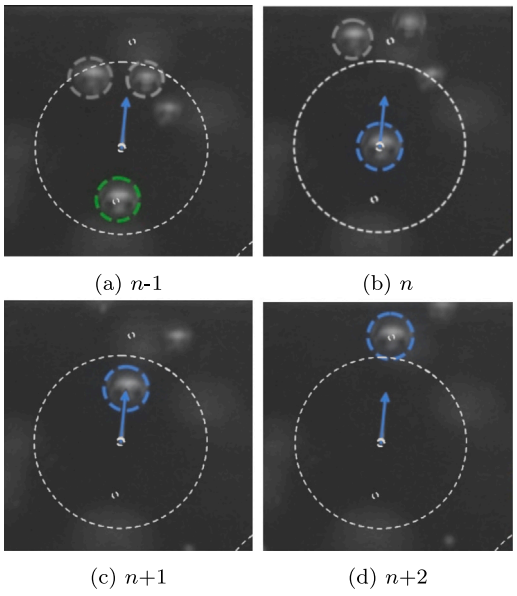

Fig. 4. Example of the four-frames, forward–backward PTV algorithm for small sections of the (a) backwards, (b) base, (c) forward and (d) two forward frames at $u_{el}^{0} = 0\,\mathrm{mm\,s^{-1}}$ and $i = 0.1\,\mathrm{A\,cm^{-2}}$.

Fig. 4 provides an exemplary illustration of the algorithm at four small sections of consecutive frames that are taken in the middle viewing panel at $u_{el}^{0} = 0\,\mathrm{mm\,s^{-1}}$ and $i = 0.1\,\mathrm{A\,cm^{-2}}$. In order to visualize the results of the PTV measurement over different bubble sizes, the determined velocities are sorted into bins with a width of 100 µm of their associated diameter. For each bin, the arithmetic mean, and $u_{b,\min}, u_{b,25}, u_{b,50}, u_{b,75}$ and $u_{b,\max}$ for box plots are calculated if at least 100 pairs of velocity and diameter are detected for the size bin. The R-CNN and the combined PTV algorithm are publicly available (Sibirtsev, 2022).

When applying a PTV algorithm on images, velocity measurement errors arise from position uncertainty and acceleration (Feng et al., 2011). Position uncertainties stem from the particle positions $\boldsymbol{x}$ that are then used to calculate the velocity. Random noise in the images, errors in the bounding boxes introduced by our R-CNN algorithm, and the finite pixel size of the camera sensor introduce an error that can be estimated by $\epsilon_{pos}^{2} = 2 \cdot \boldsymbol{x}^{2}/\Delta t^{2}$ (Feng et al., 2011). Using our camera settings, a deviation of one pixel corresponds to an absolute error of $1.41\,\mathrm{mm\,s^{-1}}$. For example, the resulting relative error for an average velocity of $40\,\mathrm{mm\,s^{-1}}$ would amount 3.5% but becomes increasingly larger for smaller velocities. Particle acceleration errors are only relevant if a particulate tracer is applied to measure the velocity of a continuous (electrolyte) phase. The error quantifies possible deviations of the velocity of the particulate tracer and the continuous phase due to the de- and acceleration of the tracer particles. In this study, we applied the PTV algorithm to measure the velocity of the dispersed bubble phase. Hence, this error becomes zero.

3. Results and discussion

Depending on i, u_{el}^{0} and examined viewing panel, between 20,000 and 150,000 bubble trajectories are determined by the PTV algorithm and on average, each experiment yields 73,000 velocity vectors. Throughout all experiments, the vertical velocity follows a Gaussian distribution. Exemplary, Fig. 5 shows the measured velocity distribution and the corresponding fitted normal distribution at the middle viewing panel at $i = 0.1\,\mathrm{A\,cm^{-2}}$ and $u_{el}^{0} = 0\,\mathrm{mm\,s^{-1}}$. The measured velocities closely follow a normal distribution and the arithmetic mean μ and standard deviation σ of the velocity amount to 43.9 and 13.1 $\mathrm{mm\,s^{-1}}$, respectively. Due to the applied lower threshold of the velocity $r_{1,\min}$, no velocities below $5\,\mathrm{mm\,s^{-1}}$ are recorded. Using the cumulative normal distribution function for error estimation, this threshold introduces an error of 0.1% in this example.

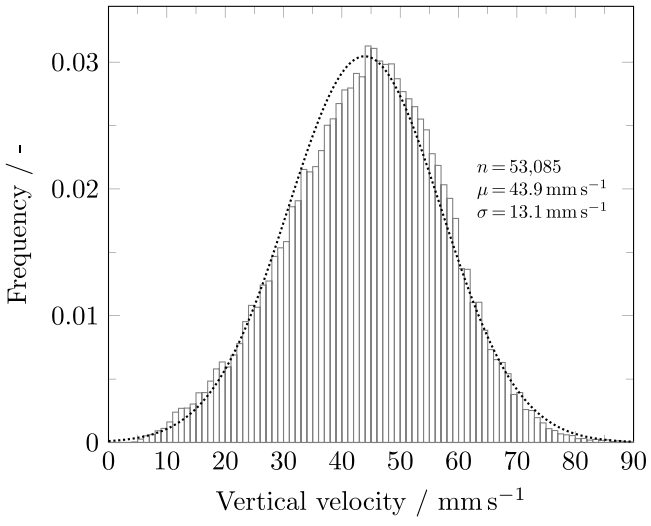

Fig. 5. Distribution of vertical velocity at the middle viewing panel for $i = 0.1\,\mathrm{A\,cm^{-2}}$ and $u_{el}^{0} = 0\,\mathrm{mm\,s^{-1}}$.

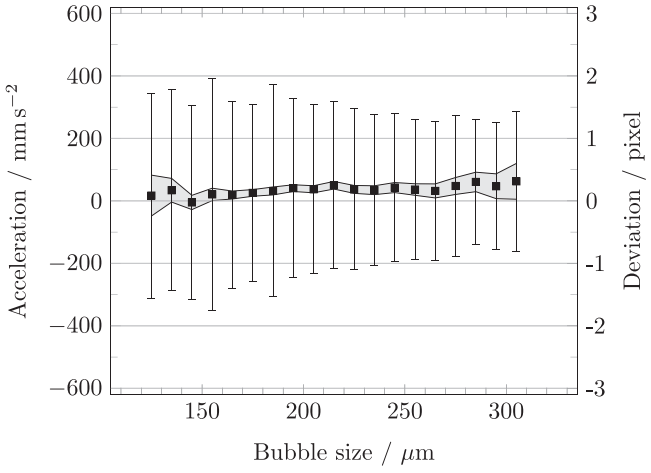

Fig. 6. Calculated average acceleration for each bubble size bin at the middle viewing panel for $i = 0.1\,\mathrm{A\,cm^{-2}}$ and NNF condition. The gray area displays the 99% confidence interval of the average acceleration. The right y-axis indicates the deviation between to subsequent trajectories of a tracked bubble in pixel.

By analyzing all particle objects that were tracked over a series of at least five frames, we estimated the change in velocity due to position uncertainty. The mean average velocity deviation and the 99% confidence interval are calculated for each size bin and displayed alongside the standard deviation in Fig. 6. For all size bins, the largest mean acceleration is smaller than $56\,\mathrm{mm\,s^{-2}}$. With the chosen frame rate and pixel size, this corresponds to a deviation between the two measured trajectories smaller than 0.5 pixels. Thus, the measured bubbles experience little to no acceleration between two measurements. Further, the shown standard deviations depict that the difference of 68% subsequently measured vertical velocities fall in between ±2 pixels. As a result, ϵ_{pos} is estimated to be smaller than $0.71\,\mathrm{mm\,s^{-2}}$. Additionally, we have not found a connection between the vertical position and velocity of the bubbles, indicating that the bubble is at terminal vertical velocity during the ascend inside the 10 mm viewing panel.

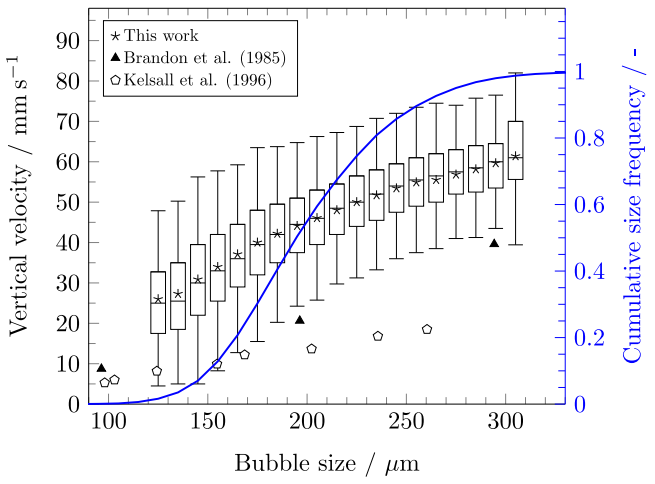

Fig. 7. Distribution of the vertical velocity against different bubble sizes and cumulative bubble size distribution (blue) at the middle viewing panel, $i = 0.1\,\mathrm{A\,cm^{-2}}$ and NNF condition. For comparison, terminal velocities of single oxygen bubbles, measured by Brandon et al. (1985) and Kelsall et al. (1996), are added. (For interpretation of the references to color in this figure legend, the reader is referred to the web version of this article.)

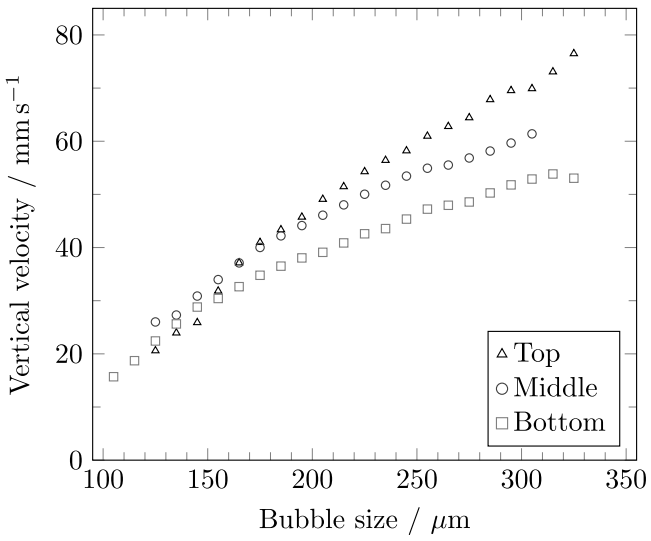

Fig. 8. Comparison of the average vertical velocity at the three different viewing panels, bottom, middle and top, at $i = 0.1\,\mathrm{A\,cm^{-2}}$ and NNF condition.

3.1. Bubble velocity versus bubble size

Box plots of the vertical velocity for different bubble size bins at the middle viewing panel are presented in Fig. 7 for $i = 0.1\,\mathrm{A\,cm^{-2}}$ and NNF conditions. On the right y-axis, the cumulative bubble size distribution is displayed. For bubble size bins between 130 and 310 μm, sufficient velocity trajectories are recorded to calculate and show the velocity distribution. The median velocity of the smallest bubbles with a size of 100 to 110 μm is 26 mm s^{-1} and the velocity exhibits a logarithmic growth with respect to the bubble size. The bin containing the mean size (190–200 μm) has an average vertical velocity of 44.1 mm s^{-1} and large bubbles with sizes greater than 300 μm show velocities up to 82 mm s^{-1}. For comparison, the terminal rising velocities of single, electrogenerated oxygen bubbles, measured by Brandon et al. (1985) and Kelsall et al. (1996), are added to Fig. 7. The determined mean vertical velocities of our work exceed the vertical rising velocities reported by Kelsall et al. (1996) and Brandon et al. (1985) by constant offsets of roughly 20 mm s^{-1} and 30 mm s^{-1}, respectively. These differences in the determined velocity between our and single-bubble experiment stem from the bubbles moving up either in a swarm inside the gas-evolving parallel plate electrolyzer or as a single bubble in a stationary electrolyte. Typically, in single-bubble experiments, the vertical velocity correlates linearly with the bubble size (Tanaka et al., 2005). Contrarily, the velocity of each bubble inside a parallel plate electrolyzer is affected by the momentum of the surrounding bubbles and the accelerated electrolyte. As most bubbles rise close to the electrode, the acceleration of the electrolyte is particularly high inside this area. This local electrolyte velocity is affected by the momentum of the whole bubble swarm consisting of different-sized bubbles. Ultimately, this leads to a greater velocity of smaller bubbles by the enhanced momentum of the electrolyte due to larger bubbles. Additionally, the effect of the accelerated electrolyte on larger bubbles is smaller, resulting in the asymptotic pattern for u_b at larger d_b.

The width of the velocity distribution remains almost constant between a bubble size of 190 and 300 μm at 37 ± 3 mm s^{-1} and widens for smaller (47 ± 3 mm s^{-1}) and the largest bubble sizes (43 mm s^{-1}). The widening of the distribution of the largest and smallest size bins partially stems from the sheer smaller sample number, as indicated by the cumulative size frequency. Additionally, if the absolute difference of a single bubble from the mean velocity increases, the more likely a collision with another bubble becomes, accelerating or slowing down the single bubble.

3.2. Bubble velocity at different heights

To investigate the effect of an increasing height and, thereby, rise in gas fraction, the bubble velocity is examined at the three viewing panels. The resulting average vertical velocities for the bottom, middle and top panels are plotted against the different bubble sizes in Fig. 8 at $i = 0.1\,\mathrm{A\,cm^{-2}}$ and $u_{el}^{0} = 0\,\mathrm{mm\,s^{-1}}$. For bubbles with a size up to 150 μm, the difference in the mean bubble velocity between the viewing panels is marginal. With an increase in bubble size, the differences between the bottom, middle and top panels enlarge: At 190 μm, the mean velocity at the bottom panel amounts to 39 mm s^{-1} and is 6 mm s^{-1} smaller than at the middle and top panels. For sizes above 200 μm, the mean velocity of the middle and top panel start to diverge, and at sizes between 290 and 300 μm, the corresponding mean velocity for bottom, middle and top amounts 53, 60 and 70 mm s^{-1}, respectively. Each size bin's relative standard deviation decreases independent of the examined viewing panel from roughly 40% at small bubble sizes to 13% for large bubbles and is supplied in the Supporting Information.

The mean and standard deviation of the velocity and size of all detected bubbles are presented in Table 3. Over the height of the three viewing panels, the bubble size stays almost constant. The maximum variation of the average bubble size is 15 μm and compared to $\sigma(d_b)$ small. Additionally, as discussed in Section 3 and shown in Fig. 6, the bubbles are not accelerated while passing the viewing panel and can be regarded as being at terminal rise velocity. Comparing the viewing panels at $i = 0.01$ and $0.05\,\mathrm{A\,cm^{-2}}$ yields similar results and is supplied in the Supporting Information. Hence, we conclude that the gain in velocity mainly stems from the increase in gas fraction and, thereby, linked electrolyte acceleration over the electrode height. By comparing only bubbles within a certain size range, we exclude the impact of the bubble size on the comparison of the vertical velocity at different operating condition. The change in the bubble Reynolds number and, thereby linked, experienced drag arises solely from the local relative velocity and swarm effects.

Our findings are in accordance with previous works: In a small electrochemical cell, u_b increases alongside the active electrode surface but remains constant above the electrode as the gas fraction stays constant (Boissonneau and Byrne, 2000) and, thus, the electrolyte velocity stays constant. At comparable heights to the bottom and middle viewing panel of this study and $i = 0.1\,\mathrm{A\,cm^{-2}}$, Abdelouahed et al. (2014a) have reported mean velocities of 17 and 20 mm s^{-1} for oxygen bubbles with a mean size of 120 μm in a latern blade electrode. Their

Table 3
Arithmetical mean μ and standard deviation σ for the bubble size and velocity at the three different viewing panels at $i = 0.1\,\mathrm{A\,cm^{-2}}$ and NNF condition.

Panel	$\mu(d_b)$ (µm)	$\sigma(d_b)$ (µm)	$\mu(v_b)$ (mm s^{-1})	$\sigma(v_b)$ (mm s^{-1})
Top	211	40	49.6	16.9
Middle	196	34	43.86	13.1
Bottom	207	39	39.51	10.04

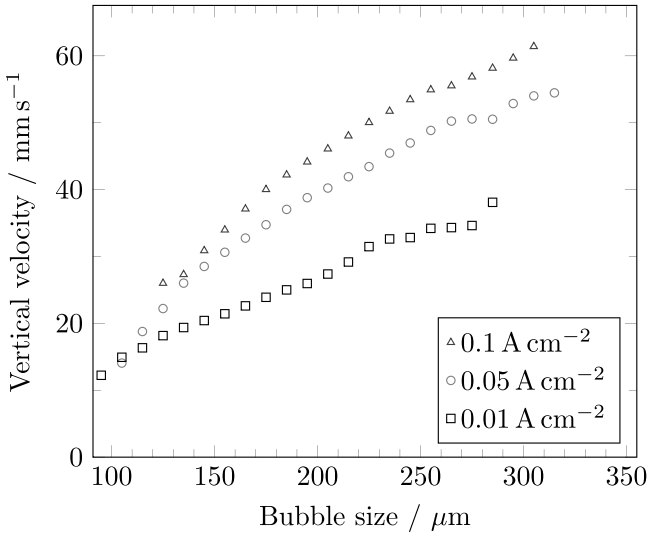

Fig. 9. Comparison of the average vertical velocity at the middle viewing panels at different $i = 0.01$, 0.5 and 0.1 A cm^{-2} and NNF condition.

values are within the standard deviation of our measured velocities 22 ±8 mm s^{-1} for bubbles with $d_b = 120$ µm.

3.3. Impact of current density on bubble velocity

The impact of three different current densities and, hence, production rates of electrogenerated oxygen on the measured vertical velocities for gas bubbles with distinct sizes between 100 and 310 µm are displayed in Fig. 9. At all three current densities, the vertical velocity increases with respect to the bubble size. At the lowest current density of 0.01 A cm^{-2}, the correlation between the vertical velocity and bubble size resembles a linear relation. In contrast, for 0.05 A cm^{-2} and 0.1 A cm^{-2}, the slope of the curve decreases at greater bubble sizes. By enlarging the current density, the mean bubble velocity increases: For bubble sizes between 120 and 130 µm, the mean vertical velocity at the middle viewing panel amounts to 18.2, 22.2 and 26 mm s^{-1} for i = 0.01, 0.05 and 0.1 A cm^{-2}, respectively. At greater bubble sizes between 250 and 260 µm, the difference between the mean vertical velocities increases, and the mean values amount 34.2, 48.8 and 54.9 mm s^{-1}.

Similar to the findings discussed in the previous section, 3.2, our results reveal the strong dependence of the vertical bubble velocity on the gas phase fraction. The mean vertical velocity of bubbles with a size of 150 µm at $i = 0.1\,\mathrm{A\,cm^{-2}}$ is almost the same as bubbles twice the size at $i = 0.01\,\mathrm{A\,cm^{-2}}$. By increasing $\dot{V}_g$, the local velocity of the electrolyte increases alongside with the mean size of all detected bubbles that amounts 182 µm at $i = 0.01\,\mathrm{A\,cm^{-2}}$, 196 µm at $i = 0.05\,\mathrm{A\,cm^{-2}}$, and 205 µm at $i = 0.1\,\mathrm{A\,cm^{-2}}$. This increase in d_b with greater i has also been shown in previous studies (Janssen et al., 1984; Görtz et al., 2024).

The measured vertical velocities fall below the ones measured by Boissonneau and Byrne (2000). For NNF conditions, they report mean velocities of electrogenerated hydrogen bubbles of 50 mm s^{-1} at i = 0.05 A cm^{-2} and 70 mm s^{-1} at $i = 0.1\,\mathrm{A\,cm^{-2}}$, whereas we determined mean vertical bubble velocities of 38 mm s^{-1} and 44 mm s^{-1}, respectively. Unfortunately, the comparability of both results is low due to the use of different parallel plate electrolyzer setups and type of gas. Contrary to our membrane-separated parallel plate electrolyzer, Boissonneau and Byrne (2000) employed an membraneless electrolyzer, in which the electrogenerated oxygen and hydrogen bubbles mixed and both affected the electrolyte flow, preventing an accurate reporting of oxygen and hydrogen bubble diameter and velocity.

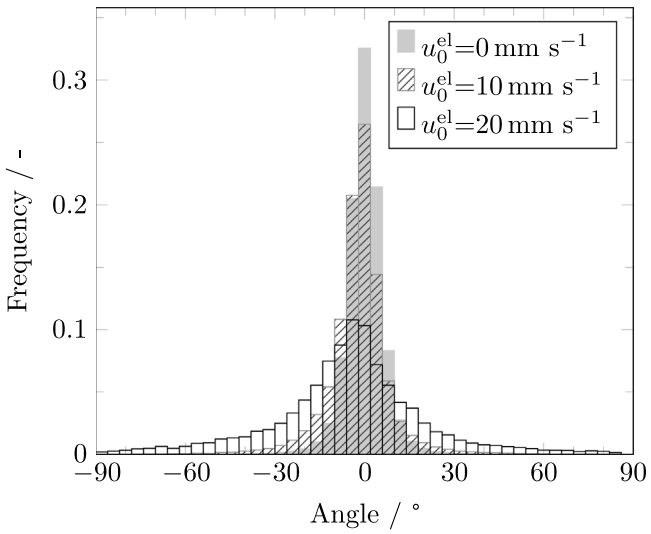

Fig. 10. Direction of bubble velocity at different u_{el}^0 = 0, 10, 20 and $i = 0.1\,\mathrm{A\,cm^{-2}}$. An angle of 0° corresponds to a straight vertical velocity.

3.4. No net flow versus forced convective flow

By applying different volumetric flow rates through the peristaltic pumps, we set u_{el}^0 to 10 and 20 mm s^{-1} and switch the operating mode of the parallel plate electrolyzer to FCF. Due to the FCF condition, the direction of the bubble velocity changes: For comparison, the measured angles of the velocity vectors are combined for all viewing panels and displayed in Fig. 10 at $i = 0.1\,\mathrm{A\,cm^{-2}}$, u_{el}^0 = 0, 10 and 20 mm s^{-1}. Here, an angle of 0° corresponds to a straight upwards trajectory. Without forced convection of the electrolyte, the majority of bubbles moves straight up: The mean angle amounts −0.1° and the standard deviation 6.5°, resulting in 95% of the bubbles rising vertically up between an angle of ±12.8°. With u_{el}^0 = 10 mm s^{-1}, the distribution of the angle widens. The standard deviation increases to 11.4°, whereas the mean angle shifts slightly to the right (1.9°). The results from the experiments with u_{el}^0 = 20 mm s^{-1} continue this trend and the angle widens further. At this condition, the mean value and standard deviation amount to 11° and 23.7°, respectively. Typically, the mean angle should be close to zero, but the shift to the right at u_{el}^0 = 20 mm s^{-1} also occurs at smaller i.

Next, the impact of different u_{el}^0 on u_b is evaluated. Fig. 11 shows the mean vertical bubble velocity and corresponding standard deviation for bubbles with diameters between 210–220 µm at i = 0.01, 0.05 and 0.1 A cm^{-2} and different u_{el}^0. For comparison, the vertical velocity under NNF condition from Section 3.3 is added to Fig. 11. The size bin was chosen for comparison as it contains the mean bubble size over all nine experiments. At $i = 0.1\,\mathrm{A\,cm^{-2}}$, the average velocity of the examined bubble size bin remains constant at around 48 mm s^{-1} up to u_{el}^0 = 10 mm s^{-1} and decreases to 18 mm s^{-1} at u_{el}^0 = 20 mm s^{-1}. In comparison, the decline of u_b at $i = 0.5\,\mathrm{A\,cm^{-2}}$ already starts at u_{el}^0 = 10 mm s^{-1}, where the average u_b reduces from 42 to 35 mm s^{-1}. Ultimately, at u_{el}^0 = 20 mm s^{-1}, u_b amounts 18.5 mm s^{-1} on average. At the smallest $i = 0.01\,\mathrm{A\,cm^{-2}}$, the average vertical u_b remains at around 27 mm s^{-1}, independent of u_{el}^0.

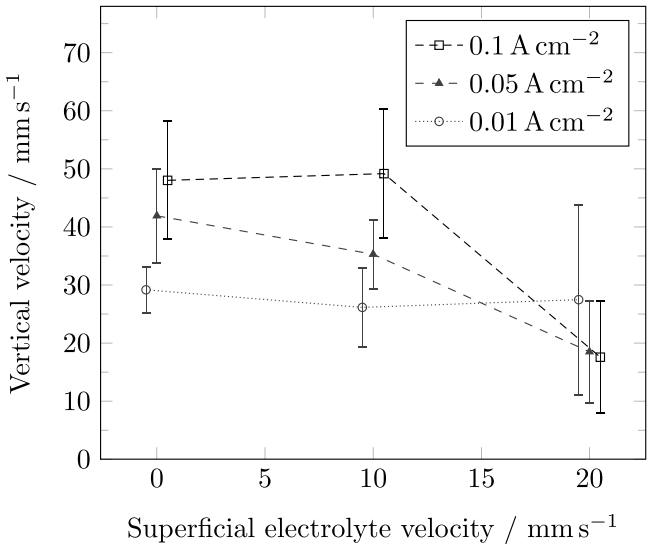

Fig. 11. Comparison of the average vertical velocity in the middle viewing panels at different $i = 0.01$, 0.5 and 0.1 A cm^{-2} and $u^0_{el} = 0$, 10 and 20 mm s^{-1} for bubbles with $d_b = 210$–220 µm. To enhance readability, the curves for $i = 0.01$ and 0.1 A cm^{-2} are slightly shifted.

Three effects can lead to the observed widening of the angle distribution and decrease in vertical velocity: (i) As proposed by Abdelouahed et al. (2014b), the flow pattern changes from 'quasi-steady' to 'transitional' with increasing u^0_{el}. By changing the flow pattern, the two vertical regimes of the flow pattern (compare Fig. 1(a)) of the bubble curtain starts to break up and single bubbles move away from the electrode, escaping into the bulk electrolyte. Thereby, the bubble's experienced relative velocity, local gas volume fraction and drag alter. Besides u^0_{el}, this change in flow pattern largely depends on i, explaining the different behavior for $i = 0.01$, 0.5 and 0.1 A cm^{-2}. Even though the Reynolds number calculated with the u^0_{el} and the hydraulic diameter is 294 and indicates a laminar flow, the electrolyte velocity in the proximity of the electrode is likely to be greater and, thus, a higher Reynolds number is to be expected. (ii) Using peristaltic pumps to generate the forced convection, the electrolyte is non-continuously pushed and, hence, the bubbles experience oscillation (Bar-Eli, 1985). Due to the periodic push–stop–push motion, the bubbles start to move horizontally, increasing the measured angle. This horizontal bubble motion disrupts the straight upward flow of the electrolyte at the electrode, increases the drag force and subsequently decreases the vertical bubble velocity. (iii) As depicted in Fig. 1, with NNF, the rising bubbles create a backflow in the bulk electrolyte that further increase the electrolyte velocity close to the electrode (Aldas et al., 2008; Hreiz et al., 2015b; Alexiadis et al., 2012). Applying a convective electrolyte flow disturbs this electrolyte backflow as the bulk electrolyte flows upwards through the parallel plate electrolyzer. Hence, the bubble curtain widens, reducing and the local gas volume fraction close to the electrode and, ultimately, decreasing the mean u_b.

4. Conclusion

The motion of electrogenerated bubbles is critical for understanding two-phase flow behavior inside parallel plate electrolyzers. Our study successfully applied a modified PTV algorithm on images taken by a high-speed camera in our previously developed, specifically designed parallel-plate electrolyzer to measure the bubble velocity and size simultaneously. Our established method enables the comparison of velocity at defined bubble sizes. Over all bubble sizes, the measured vertical velocity closely follows a normal distribution, and we observed no significant acceleration or measurement error of the analyzed bubbles. Instead of a linear linkage, the mean velocity shows a logarithmic increase with respect to bubble size, exceeding the value of experiments and correlation for a single bubble ascend. The high gas fraction close to the electrode increases the vertical velocity. We showed that small bubbles are three times as fast as single bubble experiments and that higher gas fractions that arise at greater electrode heights or larger current densities enlarge the mean vertical velocity. The linked electrolyte acceleration also affects the velocity of larger bubbles, as the experienced drag is a quadratic function of the relative velocity. By switching the operating mode from NNF to FCF, the vertical bubble velocity decreases with greater superficial electrolyte velocity at different current densities. This change in vertical bubble velocity stems from the widening of the bubble curtain and the increase in horizontal movement due to the applied convection.

Our results allow for an in-depth comparison with multiphase models to describe the gas-liquid flow in parallel plate electrolyzers by decoupling the effect of bubble size from its velocity at different operating conditions. Additionally, the presented results highlight the limited applicability of the frequently used Nicklin equation for the description of gas-liquid flows in electrolysis cells: As the equation is capable of capturing the increase in bubble velocity for higher gas fractions, our results contradict the assumption that the absolute bubble velocity increases by the amount of applied superficial electrolyte velocity under FCF conditions. Hence, to predict the bubble velocity and break up of the segregated gas-liquid flow, models have to account for the spatial distribution of the bubbles.

List of abbreviations

CFD	Computational fluid dynamics
FCF	Forced convective flow
H_2SA	Succinic acid
LDV	Laser Doppler velocimetry
Na_2SA	Di-sodium succinic acid
Na_2SO_4	Sodium sulfate
NNF	No net flow
R-CNN	Region-based convolutional neural networks
PIV	Particle image velocimetry
PTV	Particle tracking velocimetry

Mathematical symbols

a	Acceleration (m s^{-2})
d	Diameter (µm)
i	Current Density (A cm^{-2})
u	Velocity (m s^{-1})
u^0	Superficial velocity (m s^{-1})
$\dot{V}$	Gas production rate (m^3 s^{-1})
$\boldsymbol{x}$	Particle position
x	Width of bounding box (µm)
y	Height of bounding box (µm)

Greek symbols

α	Angle of ascent
Δt	Time interval between two consecutive frames
ϵ_{pos}	Velocity error due position uncertainty (m s^{-1})
μ	Mean value
σ	Standard deviation

Subscripts

b	Bubble
el	Electrolyte
g	Gas
n	Frame number
sw	Swarm

CRediT authorship contribution statement

Jonas Görtz: Conceptualization, Visualization, Writing – original draft, Writing – review & editing. **Jakob Seiler:** Formal analysis, Methodology. **Andreas Jupke:** Conceptualization, Funding acquisition.

Declaration of competing interest

The authors declare the following financial interests/personal relationships which may be considered as potential competing interests: Jonas Goertz reports financial support was provided by Federal Ministry of Education and Research Berlin Office.

Data availability

Data will be made available on request.

Acknowledgments

The authors gratefully acknowledge the financial support of "ZeTA" as part of the framework "Modellregion, BioRevierPLUS: InBio, Innovationscluster Integrierte Bioraffinerie, TP2" (no. 031B1135B/031B1135BX), supported by the Federal Ministry of Education and Research (BMBF) and the project supervision by the project management organization Projektträger Julich (PtJ).

Simulations were performed with computing resources granted by RWTH Aachen University under project rwth1276. CLAIX-2018-GPU Nodes with NVIDIA Volta 100 GPUs and 16 GB VRAM were used. Additionally, the authors would like to thank Stine Kuhlemann for her assistance in the laboratory.

Appendix A. Supplementary data

Supplementary material related to this article can be found online at https://doi.org/10.1016/j.ijmultiphaseflow.2024.104849.

References

Abdelouahed, L., 2013. Conception optimale de l'anode d'une cellule de production de fer par voie électrochimique, CFM 2013 - 21ème Congrès Français de Mécanique. Bordeaux, France. hal-03441410.

Abdelouahed, L., Hreiz, R., Poncin, S., Valentin, G., Lapicque, F., 2014a. Hydrodynamics of gas bubbles in the gap of lantern blade electrodes without forced flow of electrolyte: Experiments and CFD modelling. Chem. Eng. Sci. 111, 255–265. http://dx.doi.org/10.1016/j.ces.2014.01.028, URL: https://linkinghub.elsevier.com/retrieve/pii/S0009250914000384.

Abdelouahed, L., Valentin, G., Poncin, S., Lapicque, F., 2014b. Current density distribution and gas volume fraction in the gap of lantern blade electrodes. Chem. Eng. Res. Des. 92 (3), 559–570. http://dx.doi.org/10.1016/j.cherd.2013.10.003, URL: https://linkinghub.elsevier.com/retrieve/pii/S0263876213003997.

Aldas, K., Pehlivanoglu, N., Mat, M., 2008. Numerical and experimental investigation of two-phase flow in an electrochemical cell. Int. J. Hydrogen Energy 33 (14), 3668–3675. http://dx.doi.org/10.1016/j.ijhydene.2008.04.047, URL: https://linkinghub.elsevier.com/retrieve/pii/S0360319908004734.

Alexiadis, A., Dudukovic, M.P., Ramachandran, P., Cornell, A., 2012. On the stability of the flow in multi-channel electrochemical systems. J. Appl. Electrochem. 42 (9), 679–687. http://dx.doi.org/10.1007/s10800-012-0426-0, URL: http://link.springer.com/10.1007/s10800-012-0426-0.

Alexiadis, A., Dudukovic, M., Ramachandran, P., Cornell, A., Wanngård, J., Bokkers, A., 2011a. Liquid–gas flow patterns in a narrow electrochemical channel. Chem. Eng. Sci. 66 (10), 2252–2260. http://dx.doi.org/10.1016/j.ces.2011.02.046, URL: https://linkinghub.elsevier.com/retrieve/pii/S0009250911001412.

Alexiadis, A., Dudukovic, M.P., Ramachandran, P., Cornell, A., Wanngård, J., Bokkers, A., 2011b. On the electrode boundary conditions in the simulation of two phase flow in electrochemical cells. Int. J. Hydrogen Energy 36 (14), 8557–8559. http://dx.doi.org/10.1016/j.ijhydene.2011.04.149.

Bar-Eli, K., 1985. The peristaltic effect on chemical oscillations. J. Phys. Chem. 89 (13), 2852–2855. http://dx.doi.org/10.1021/j100259a029, URL: https://pubs.acs.org/doi/10.1021/j100259a029.

Boissonneau, P., Byrne, P., 2000. An experimental investigation of bubble-induced free convection in a small electrochemical cell. J. Appl. Electrochem. 30 (7), 767–775. http://dx.doi.org/10.1023/A:1004034807331, URL: http://link.springer.com/10.1023/A:1004034807331.

Brandon, N.P., Kelsall, G.H., Levine, S., Smith, A.L., 1985. Interfacial electrical properties of electrogenerated bubbles. J. Appl. Electrochem. 15 (4), 485–493. http://dx.doi.org/10.1007/BF01059289, URL: http://link.springer.com/10.1007/BF01059289.

Bruggeman, D.A.G., 1935. Berechnung verschiedener physikalischer Konstanten von heterogenen Substanzen. I. Dielektrizitätskonstanten und Leitfähigkeiten der Mischkörper aus isotropen Substanzen. Ann. Phys., Lpz. 416 (7), 636–664. http://dx.doi.org/10.1002/andp.19354160705, URL: https://onlinelibrary.wiley.com/doi/10.1002/andp.19354160705.

Cheng, W., Murai, Y., Sasaki, T., Yamamoto, F., 2005. Bubble velocity measurement with a recursive cross correlation PIV technique. Flow Meas. Instrum. 16 (1), 35–46. http://dx.doi.org/10.1016/j.flowmeasinst.2004.08.002, URL: https://linkinghub.elsevier.com/retrieve/pii/S0955598604000597.

Davis, J.T., Brown, D.E., Pang, X., Esposito, D.V., 2019. High speed video investigation of bubble dynamics and current density distributions in membraneless electrolyzers. J. Electrochem. Soc. 166 (4), F312–F321. http://dx.doi.org/10.1149/2.0961904jes, URL: https://iopscience.iop.org/article/10.1149/2.0961904jes.

Eigeldinger, J., Vogt, H., 2000. The bubble coverage of gas-evolving electrodes in a flowing electrolyte. Electrochim. Acta 45 (27), 4449–4456. http://dx.doi.org/10.1016/S0013-4686(00)00513-2, URL: https://linkinghub.elsevier.com/retrieve/pii/S0013468600005132.

Feng, Y., Goree, J., Liu, B., 2011. Errors in particle tracking velocimetry with high-speed cameras. Rev. Sci. Instrum. 82 (5), 053707. http://dx.doi.org/10.1063/1.3589267, URL: http://aip.scitation.org/doi/10.1063/1.3589267.

Fuller, T.F., Harb, J.N., 2018. Electrochemical Engineering, first ed. Wiley, Hoboken, NJ, USA.

Görtz, J., Seiler, J., Kolmer, P., Jupke, A., 2024. Raising the curtain: Bubble size measurement inside parallel plate electrolyzers. Chem. Eng. Sci. 286, 119550. http://dx.doi.org/10.1016/j.ces.2023.119550, URL: https://linkinghub.elsevier.com/retrieve/pii/S0009250923011065.

Hreiz, R., Abdelouahed, L., Fünfschilling, D., Lapicque, F., 2015a. Electrogenerated bubbles induced convection in narrow vertical cells: A review. Chem. Eng. Res. Des. 100, 268–281. http://dx.doi.org/10.1016/j.cherd.2015.05.035, URL: https://linkinghub.elsevier.com/retrieve/pii/S0263876215001963.

Hreiz, R., Abdelouahed, L., Fünfschilling, D., Lapicque, F., 2015b. Electrogenerated bubbles induced convection in narrow vertical cells: PIV measurements and Euler–Lagrange CFD simulation. Chem. Eng. Sci. 134, 138–152. http://dx.doi.org/10.1016/j.ces.2015.04.041, URL: https://linkinghub.elsevier.com/retrieve/pii/S0009250915003024.

Ilonen, J., Juránek, R., Eerola, T., Lensu, L., Dubská, M., Zemčík, P., Kälviäinen, H., 2018. Comparison of bubble detectors and size distribution estimators. Pattern Recognit. Lett. 101, 60–66. http://dx.doi.org/10.1016/j.patrec.2017.11.014, URL: https://linkinghub.elsevier.com/retrieve/pii/S0167865517304282.

Janssen, L., 1978. Mass transfer at gas evolving electrodes. Electrochim. Acta 23 (2), 81–86. http://dx.doi.org/10.1016/0013-4686(78)80101-7, URL: https://linkinghub.elsevier.com/retrieve/pii/0013468678801017.

Janssen, L., Sillen, C., Barendrecht, E., van Stralen, S., 1984. Bubble behaviour during oxygen and hydrogen evolution at transparent electrodes in KOH solution. Electrochim. Acta 29 (5), 633–642. http://dx.doi.org/10.1016/0013-4686(84)87122-4, URL: https://linkinghub.elsevier.com/retrieve/pii/0013468684871224.

Kelsall, G.H., Tang, S., Smith, A.L., Yurdakul, S., 1996. Measurement of rise and electrophoretic velocities of gas bubbles. J. Chem. Soc. Faraday Trans. 92 (20), 3879. http://dx.doi.org/10.1039/ft9969203879, URL: http://xlink.rsc.org/?DOI=ft9969203879.

Kreysa, G., Kuhn, M., 1985. Modelling of gas evolving electrolysis cells. I. The gas voidage problem. J. Appl. Electrochem. 15 (4), 517–526. http://dx.doi.org/10.1007/BF01059293, URL: http://link.springer.com/10.1007/BF01059293.

Kuroda, I., Sakakibara, A., Sasaki, T., Murai, Y., Nagai, N., Yamamoto, F., 2008. PIV study on buoyant bubble flows in a small electrolytic cell. Jpn. J. Multiph. Flow 22 (2), 161–174. http://dx.doi.org/10.3811/jjmf.22.161, URL: http://www.jstage.jst.go.jp/article/jjmf/22/2/22_2_161/_article.

Liu, L., Cai, W., Chen, Y., Wang, Y., 2018. Fluid dynamics and mass transfer study of electrochemical oxidation by CFD prediction and experimental validation. Ind. Eng. Chem. Res. 57 (18), 6493–6504. http://dx.doi.org/10.1021/acs.iecr.7b04226.

Liu, C.-L., Sun, Z., Lu, G.-M., Song, X.-F., Yu, J.-G., 2015. Experimental and numerical investigation of two-phase flow patterns in magnesium electrolysis cell with non-uniform current density distribution. Can. J. Chem. Eng. 93 (3), 565–579. http://dx.doi.org/10.1002/cjce.22135, URL: https://onlinelibrary.wiley.com/doi/10.1002/cjce.22135.

Mandin, P., Aissa, A.A., Roustan, H., Hamburger, J., Picard, G., 2008. Two-phase electrolysis process: From the bubble to the electrochemical cell properties. Chem. Eng. Process.: Process Intensif. 47 (11), 1926–1932. http://dx.doi.org/10.1016/j.cep.2007.10.018.

Mat, M., Aldas, K., 2005. Application of a two-phase flow model for natural convection in an electrochemical cell. Int. J. Hydrogen Energy 30 (4), 411–420. http://dx.doi.org/10.1016/j.ijhydene.2004.04.002, URL: https://linkinghub.elsevier.com/retrieve/pii/S036031990400179X.

Nicklin, D., 1962. Two-phase bubble flow. Chem. Eng. Sci. 17 (9), 693–702. http://dx.doi.org/10.1016/0009-2509(62)85027-1, URL: https://linkinghub.elsevier.com/retrieve/pii/0009250962850271.

Poletaev, I., Tokarev, M.P., Pervunin, K.S., 2020. Bubble patterns recognition using neural networks: Application to the analysis of a two-phase bubbly jet. Int. J. Multiph. Flow 126, 103194. http://dx.doi.org/10.1016/j.ijmultiphaseflow.2019.103194, URL: https://linkinghub.elsevier.com/retrieve/pii/S0301932219305701.

Pyle, D., Harrison, D., 1967. The rising velocity of bubbles in two-dimensional fluidised beds. Chem. Eng. Sci. 22 (4), 531–535. http://dx.doi.org/10.1016/0009-2509(67)80036-8, URL: https://linkinghub.elsevier.com/retrieve/pii/0009250967800368.

Rajora, A., Haverkort, J., 2022. An analytical multiphase flow model for parallel plate electrolyzers. Chem. Eng. Sci. 260, 117823. http://dx.doi.org/10.1016/j.ces.2022.117823, URL: https://linkinghub.elsevier.com/retrieve/pii/S0009250922004079.

Rajora, A., Haverkort, J., 2023. An analytical model for the velocity and gas fraction profiles near gas-evolving electrodes. Int. J. Hydrogen Energy 48 (71), 27450–27463. http://dx.doi.org/10.1016/j.ijhydene.2023.03.154, URL: https://linkinghub.elsevier.com/retrieve/pii/S0360319923012247.

Richardson, J., Zaki, W., 1954. The sedimentation of a suspension of uniform spheres under conditions of viscous flow. Chem. Eng. Sci. 3 (2), 65–73. http://dx.doi.org/10.1016/0009-2509(54)85015-9, URL: https://linkinghub.elsevier.com/retrieve/pii/0009250954850159.

Sibirtsev, S., 2022. Mask r-cnn implementation for droplet detection in liquid multiphase systems. URL: https://github.com/ssibirtsev/MRCNN-droplet-detection. Publication Title: GitHub repository.

Sibirtsev, S., Zhai, S., Neufang, M., Seiler, J., Jupke, A., 2023. Mask R-CNN based droplet detection in liquid–liquid systems, Part 2: Methodology for determining training and image processing parameter values improving droplet detection accuracy. Chemical Engineering Journal 473, 144826. http://dx.doi.org/10.1016/j.cej.2023.144826, https://linkinghub.elsevier.com/retrieve/pii/S138589472303557X.

Sigrist, L., Dossenbach, O., Ibl, N., 1979. Mass transport in electrolytic cells with gas sparging. Int. J. Heat Mass Transfer 22 (10), 1393–1399. http://dx.doi.org/10.1016/0017-9310(79)90201-1, URL: https://linkinghub.elsevier.com/retrieve/pii/0017931079902011.

Sigrist, L., Dossenbach, O., Ibl, N., 1980. On the conductivity and void fraction of gas dispersions in electrolyte solutions. J. Appl. Electrochem. 10 (2), 223–228. http://dx.doi.org/10.1007/BF00726089, URL: http://link.springer.com/10.1007/BF00726089.

Sillen, C.P., 1983. The effect of gas bubble evolution on the energy efficiency in water electrolysis. http://dx.doi.org/10.6100/IR40592, URL: https://research.tue.nl/en/publications/the-effect-of-gas-bubble-evolution-on-the-energy-efficiency-in-water-electrolysis(f0221d1e-d395-4145-8430-11730484eb1d).html. Publisher: Technische Hogeschool Eindhoven.

Tanaka, Y., Kikuchi, K., Saihara, Y., Ogumi, Z., 2005. Bubble visualization and electrolyte dependency of dissolving hydrogen in electrolyzed water using Solid-Polymer-Electrolyte. Electrochim. Acta 50 (25–26), 5229–5236. http://dx.doi.org/10.1016/j.electacta.2005.01.062, URL: https://linkinghub.elsevier.com/retrieve/pii/S001346860500558X.

Vogt, H., Balzer, R., 2005. The bubble coverage of gas-evolving electrodes in stagnant electrolytes. Electrochim. Acta 50 (10), 2073–2079. http://dx.doi.org/10.1016/j.electacta.2004.09.025, URL: https://linkinghub.elsevier.com/retrieve/pii/S001346860400948X.

Vukasinovic, B., Smith, M.K., Glezer, A., 2004. Spray characterization during vibration-induced drop atomization. Phys. Fluids 16 (2), 306–316. http://dx.doi.org/10.1063/1.1632907, URL: http://aip.scitation.org/doi/10.1063/1.1632907.

Wosiak, G., Silva, J.d., Sena, S.S., Carneiro-Neto, E.B., Lopes, M.C., Pereira, E., 2022. Investigation of the influence of the void fraction on the energy consumption of a vertical electrolyser under natural convection. J. Environ. Chem. Eng. 10 (3), 107577. http://dx.doi.org/10.1016/j.jece.2022.107577, URL: https://linkinghub.elsevier.com/retrieve/pii/S221334372200450X.

Zhao, X., Ren, H., Luo, L., 2019. Gas bubbles in electrochemical gas evolution reactions. Langmuir 35 (16), 5392–5408. http://dx.doi.org/10.1021/acs.langmuir.9b00119, URL: https://pubs.acs.org/doi/10.1021/acs.langmuir.9b00119.